Effect of dsDNA on the Assembly Pathway and Mechanical Strength of SV40 VP1 Virus-like Particles

van Rosmalen, Mariska G.M.; Li, Chenglei; Zlotnick, Adam; Wuite, Gijs J.L.; Roos, Wouter H.

published in
Biophysical Journal
2018

DOI (link to publisher)
10.1016/j.bpj.2018.07.044

document version
Publisher's PDF, also known as Version of record

Biophysical Journal
Article

Biophysical Society

Effect of dsDNA on the Assembly Pathway and Mechanical Strength of SV40 VP1 Virus-like Particles

Mariska G. M. van Rosmalen,[1] Chenglei Li,[2] Adam Zlotnick,[2] Gijs J. L. Wuite,[1,*] and Wouter H. Roos[3,*]
[1]Natuur- en Sterrenkunde and LaserLaB, Vrije Universiteit Amsterdam, Amsterdam, The Netherlands; [2]Department of Molecular and Cellular Biochemistry, Indiana University, Bloomington, Indiana; and [3]Moleculaire Biofysica, Zernike Instituut, Rijksuniversiteit Groningen, Groningen, The Netherlands

ABSTRACT Simian virus 40 (SV40) is a possible vehicle for targeted drug delivery systems because of its low immunogenicity, high infectivity, and high transfection efficiency. To use SV40 for biotechnology applications, more information is needed on its assembly process to efficiently incorporate foreign materials and to tune the mechanical properties of the structure. We use atomic force microscopy to determine the effect of double-stranded DNA packaging, buffer conditions, and incubation time on the morphology and strength of virus-like particles (VLPs) composed of SV40 VP1 pentamers. DNA-induced assembly results in a homogeneous population of native-like, ~45 nm VLPs. In contrast, under high-ionic-strength conditions, the VP1 pentamers do not seem to interact consistently, resulting in a heterogeneous population of empty VLPs. The stiffness of both in-vitro-assembled empty and DNA-filled VLPs is comparable. Yet, the DNA increases the VLPs' resistance to large deformation forces by acting as a scaffold, holding the VP1 pentamers together. Both disulfide bridges and Ca^{2+}, important in-vitro-assembly factors, affect the mechanical stability of the VLPs: the reducing agent DTT makes the VLPs less resistant to mechanical stress and prone to damage, whereas Ca^{2+}-chelating EDTA induces a marked softening of the VLP. These results show that negatively charged polymers such as DNA can be used to generate homogeneous particles, thereby optimizing VLPs as vessels for drug delivery. Moreover, the storage buffer should be chosen such that VP1 interpentamer interactions are preserved.

INTRODUCTION

Simian virus 40 (SV40) is a nonenveloped DNA virus with a 5.2 kbp circular double-stranded DNA (dsDNA) genome belonging to the *Polyomaviridae* family. Its capsid is ~45 nm in diameter and is made up of VP1 capsid protein, which is the major capsid protein. SV40 has been extensively studied for possible applications as a vehicle for targeted drug delivery systems. Because SV40 is nonimmunogenic and can efficiently infect a wide range of human cells, including hematopoietic stem cells, many possibilities are open for drug delivery strategies based on SV40 virus-like particles (VLPs; particles that resemble viral capsids but are noninfectious) (1–4). Furthermore, a viral-based system has the advantage of having a high transfection efficiency, and SV40 has been shown to be an efficient gene delivery system (5,6). In vitro, VP1 pentamers can assemble around different materials including foreign DNA up to 17.7 kbp and several types of artificial cargo (7–14). Also, the surface can be modified to create targeted VLPs (15–18). Tsukamoto et al. (10) examined the effect of the genome length on assembly and concluded that for assembly of complete ~40 nm VLPs, DNA of at least 250 bp incubated with VP1 pentamers for 16 h is necessary. In agreement with this study, Mukherjee et al. (19) used 600 bp DNA at different VP1 pentamer per DNA ratios and observed ~45 nm VLPs after 24 h at the ratios of 72:1 and 144:1. However, only electron microscopy images after >16 h of incubation with DNA that is smaller than the wild-type SV40 genome were reported. Thus, information regarding the assembly process as a function of time as well as how differences in cargo (e.g., DNA length) affect the assembly pathway and mechanical strength of SV40 VLPs is currently lacking. Optimizing the assembly pathway and understanding its correlation with mechanical strength will help to create a safer drug delivery system by preventing the release of the incorporated cargo before reaching its target site.

The capsid of SV40 is made up of 72 VP1 pentamers that form the $T = 7$ icosahedral capsid structure, in which the

Submitted March 5, 2018, and accepted for publication July 16, 2018.
*Correspondence: g.j.l.wuite@vu.nl or w.h.roos@rug.nl
Editor: Nancy Forde.
https://doi.org/10.1016/j.bpj.2018.07.044

pentamers fill both the pentavalent and hexavalent sites (20,21). Each VP1 pentamer has five carboxy-terminal arms that lock into a neighboring pentamer via calcium bridges and disulfide linkage (21,22). Stehle and co-workers (21) provide a clear representation of the VP1 pentamers and their interactions. Stable VP1 pentamers have been expressed and purified from virions and bacterial and insect cell-expression systems (23–25). It has been shown that these VP1 pentamers are able to assemble in vitro into VLPs. Assembly of purified VP1 pentamers into empty VLPs can be induced by specific buffer conditions, i.e., presence of calcium, low pH, and/or adapting the ionic strength. Also, VP1 can bind DNA nonspecifically with high affinity via its N-terminal region (26). Binding of VP1 pentamers to DNA results in an increased local concentration that initiates the assembly into VLPs (10,19,27,28). SV40 virions also have a minor capsid protein VP2, or its variant VP3, that binds to the VP1 pentamer and interacts with DNA (29,30); however, VP2 is not required for in vitro assembly or DNA packaging.

Nanoindentation by atomic force microscopy (AFM) is a powerful technique to characterize the mechanical properties of nanosized systems such as viruses (31–34). With AFM imaging, one also obtains topographical information of the sample, allowing both morphological and mechanical analyses of the same nanostructure. We used AFM as an imaging tool to observe the different assembly structures of the VP1 pentamers at the nanometer scale. We used AFM nanoindentation to determine the mechanical properties of in-vitro-assembled empty and DNA-filled VLPs to assess the influence of the DNA content on their mechanical response (35–39). In addition to nucleic acid content, we explored the effect of the interpentamer interactions, i.e., disulfide bonds and calcium bridges (21,22), by changing the buffer conditions. We expected these to have a stabilizing role on the mechanical strength of the SV40 VP1 VLPs. Furthermore, we explored the time frame of the assembly pathway. Altogether, we have shed new light, to our knowledge, on the mechanism of VLP assembly and determined the influence of DNA content and interpentamer interactions on the mechanical properties of SV40 VP1 VLPs.

MATERIALS AND METHODS

Protein and DNA for assembly reactions

SV40 VP1 VLPs were produced in *Spodoptera frugiperda* insect cells, harvested, and purified as described previously by (40). Briefly, *S. frugiperda* cells were infected with recombinant baculovirus expressing VP1. The cells were harvested 72 h postinfection, and nuclear extracts were isolated. VLPs filled with random nucleic acid were purified by two rounds of CsCl gradient centrifugation, which ensured a uniform protein/DNA ratio. Samples of DNA-filled VLPs were routinely examined by electron microscopy using 1% uranyl acetate as a negative stain and by sodium dodecyl sulfate polyacrylamide gel electrophoresis to show uniform morphology and protein purity, respectively. We used two protocols to obtain VP1 pentamers. Initially, we followed the procedure described by Li et al. (41). Briefly, DNA-filled VLPs were dissociated by dialysis against 20 mM Tris-Cl (pH 8.9), 50 mM NaCl, 2 mM dithiothreitol (DTT), and 5 mM EDTA at 4°C. The dialysate was centrifuged to remove aggregated protein and then loaded on a Superose 6 column (GE Lifesciences, Chicago, IL) equilibrated in 100 mM 3-(N-morpholino)propanesulfonic acid (MOPS; pH 7.2), 250 mM NaCl. The total protein concentration was quantified by absorbance using an extinction coefficient of ε_{280} = 32,890 M/cm per VP1 monomer, which is based on amino acid composition (42). We observed that after dialysis, there was a loss of essentially all ultraviolet absorbance, attributable to nucleic acid (43). This observation indicates that packaged nucleic acid was small enough to readily cross a dialysis membrane, at least after treatment with the basic dissociation buffer. Therefore, we eliminated the slow column step and simply subjected thawed VLPs to repeated buffer exchange into dissociation buffer. For this approach, small VLP aliquots, stored under argon at −20°C, were dissociated by adding the disassembly buffer components 20 mM TrisCl (pH 8.9), 5 mM EDTA, and 2 mM DTT to the VLPs. To ensure dissociation into pentamers, after 30 min at room temperature, samples were imaged with AFM. Then, the buffer was exchanged to assembly buffer (20–50 mM MOPS (pH 7.2), 125–150 mM NaCl, and 2 mM $CaCl_2$) by ultracentrifugation using Amicon Ultracentrifugal filters 100 k (Millipore, Burlington, MA). In the absence of high ionic strength or nucleic acid, no assembled particles were observed in these samples. For in vitro assembly experiments, only VP1 pentamers in assembly buffer were used, meaning no RNA/DNA nor other proteins nor any cellular material was present.

In vitro assembly of empty VLPs was stimulated by high ionic strength. VP1 pentamers at a concentration of 330 nM were dialyzed against a 2 M $(NH_4)_2SO_4$ solution with 20 mM MOPS (pH 7.2) and 2 mM $CaCl_2$ for 1.5–24 h at 4°C using 0.025 μm VSWP Membrane Filters (Millipore). For in vitro DNA-stimulated assembly, different DNAs at different concentrations were used. In the case of the 4361 bp plasmid pBr322 (Thermo Fisher Scientific, Waltham, MA), the assembly experiments were performed at a concentration of 10 ng/μL per 440 nM VP1 pentamers and incubated at room temperature for 2 or 24 h with and without a prior incubation step of 30 min on ice. The 3015 bp vector pGEM-T Easy Vector (Promega, Madison, WI) was used at a concentration of 5 ng/μL per 150 nM VP1 pentamers and incubated 30 min on ice followed by 2 or 24 h at room temperature. Bacteriophage λ DNA of 48,502 bp (Roche Diagnostics, Mannheim, Germany) was used at concentrations of 5–158 ng/μL DNA per 360–440 nM VP1 pentamers (72:1, 360:1, and 2750:1 ratios) and incubated at room temperature for 2, 3, 6, or 24 h or 90 min on ice followed by 2 or 24 h at room temperature. The pKYB1 vector of 8393 bp (expressed in *Escherichia coli*) was used at a concentration of 28 ng/μL DNA per 360 nM VP1 pentamers (72:1 ratio) and incubated at room temperature for 6 or 24 h.

AFM

For imaging and nanoindentation experiments, the VLPs were immobilized onto a suitable surface. For high-resolution images of the cell-derived SV40 VP1 VLPs, single VP1 pentamers, and the in-vitro-assembled empty VLPs, hydrophobic glass slides were preferred for immobilization and prepared as described previously (44). In short, first the glass slides were cleaned by incubating them overnight in an ethanol-water bath saturated with potassium hydroxide, followed by thoroughly washing them with MilliQ water and drying them by air. The cleaned glass slides were incubated overnight in hexamethyldisilazane vapor to make them hydrophobic. For immobilization of the in-vitro-assembled VLPs on oversized dsDNA substrates (pKYB1 and λ), an 3-aminopropyltriethoxysilane -functionalized (i.e., hydrophilic) mica was preferred. Freshly cleaved mica was incubated for 80 s in a 1% 3-aminopropyltriethoxysilane in ethanol solution and rinsed with acetone, 70% ethanol, and milliQ water, respectively. All VLP samples were diluted in assembly buffer (20–50 mM MOPS (pH 7.2), 125–150 mM NaCl, and 2 mM $CaCl_2$) and incubated on the preferred surface at a volume of 40–100 μL for ~15 min at room

temperature. To determine the effect of interpentamer interactions, either 2 mM DTT or 5 mM EDTA was added to the cell-derived SV40 VP1 VLPs after immobilization.

Images and nanoindentation curves were obtained with an AFM from Nanotec Electronica (Madrid, Spain) operated in jumping mode (45) at room temperature in buffer solution. Olympus OMCL-RC800PSA rectangular, silicon-nitride cantilevers with a nominal tip radius of 15 nm and a nominal spring constant of 0.05 N/m were used (Olympus, Tokyo, Japan). The average imaging force was ~200 pN, with a maximum of 386 pN. Obtained images were processed and analyzed using the WSxM software. In jumping mode, tip-sample interaction is monitored in real time while the tip is moving toward and away from the sample, meaning the tip is touching the sample. The lateral motion is done out of contact, reducing shear forces; however, the height obtained from the images needs to be corrected for the scanning force according to

$$Height_{real} = Height_{measured} + \frac{F_{imaging}}{\kappa_{virus}},$$

where $F_{imaging}$ is the imaging force and κ_{virus} the spring constant of the capsid. We observed two populations of spring constants, which are predicted to correspond to complete and damaged/incomplete VLPs (see Results). Thus, the spring constant found for the intact VLPs (0.10 ± 0.01 (SD) N/m) was used for a height correction of the VLPs with a measured height of ≥40 nm, whereas the smaller VLPs <40 nm were corrected with the spring constant (0.034 ± 0.004 (SD) N/m) observed for the damaged/incomplete VLPs.

For nanoindentations, we zoomed in on individual VLPs and positioned the tip at the center. 10 consecutive nanoindentation cycles were performed on each VLP with a ~53 nm/s loading speed and 0.3 nm step size. The obtained force-distance curves were analyzed with a home-built MATLAB program. In detail, the force-distance curves were transformed into force-indentation curves. This was done by subtracting a curve obtained on bare glass representing the elasticity of the cantilever (44). The force-indentation curve represents the relation between force and deformation of the VLP. This allowed us to use a linear fit to the first part of the force-indentation curve, from the contact point up to the first rupture event with a maximum of the thickness of the VP1 pentamers (~6 nm) (32), to determine the spring constant of the capsid. The contact point was determined using a change point method (46). For representation purposes, the contact point was used to align the entire series of 10 indentation curves on a single VLP to more clearly represent the damage inflicted throughout the consecutive indentations. Additionally, a close-up image of the VLP after indentation was obtained to determine the amount of damage inflicted by the indentations. To quantify this damage, we calculated the percentage of volume decrease. The volume of the VLPs before indentation and the volume of the remaining structure after indentation was determined using Gwyddion software. Stated error, unless specified otherwise, is the standard error of the mean.

RESULTS

Disassembly of SV40 VP1 VLPs

To obtain VP1 pentamers that could be used for our designed assembly experiments, we first needed to dissociate cell-derived SV40 VLPs. Before disassembly, the VLPs are sphere-like structures with a height of ~40–45 nm (Fig. 1, *a* and *b*). Upon addition of the buffer components known to facilitate disassembly (5 mM DTT and 5 mM EDTA in a low-ionic-strength buffer (pH 8.9) (19)), we observed immediate dissociation into single VP1 pentamers

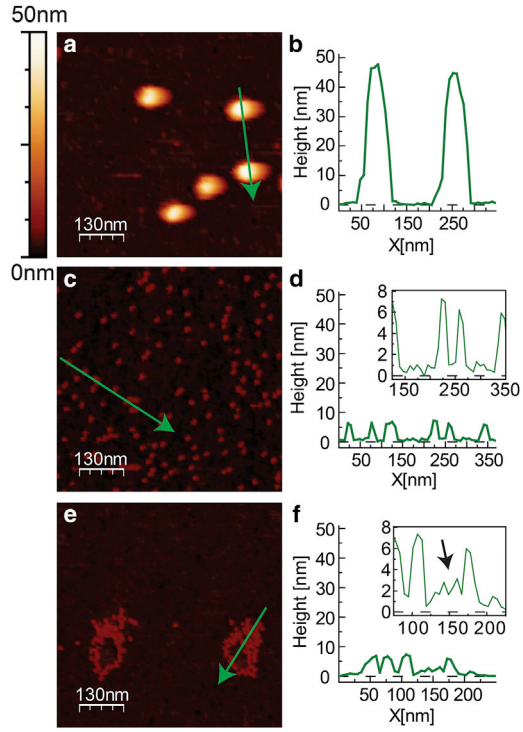

FIGURE 1 Cell-derived SV40 VLPs before and after disassembly. (*a* and *b*) A topographical AFM image of SV40 VLPs that are immobilized on hydrophobic glass is shown. The VLPs are round, with a height of 40–45 nm. (*c* and *d*) VP1 pentamers with a height of ~6 nm were obtained from VLPs by the addition of the disassembly buffer components 5 mM DTT and 5 mM EDTA in a low-ionic-strength buffer with pH 8.9. The inset shows a magnified section of (*d*). (*e* and *f*) When disassembly buffer was added to immobilized SV40 VLPs, the VLPs dissociated immediately into VP1 pentamers, forming a ring-like structure surrounding a structure resembling the DNA content (*black arrow*). To see this figure in color, go online.

(Fig. 1, *c* and *e*). With dynamic light scattering, we confirmed that the dissociation is completed within ~10 min. VP1 pentamers have a height of ~6 nm, which is in agreement with the diameter of the short axis of the pentamer crystal structure (20) (Fig. 1, *d* and *f*). When the buffer components were added while the VLPs were in solution, the VP1 pentamers randomly immobilized onto the surface, suggesting complete dissociation (Fig. 1 *c*). Interestingly, when the buffer components were added to immobilized VLPs, we observed VP1 pentamers in a ring with a lower height structure (~2 nm) in the middle (Fig. 1, *e* and *f*). The height of the 2 nm structure in the middle fits with the size of DNA (47,48). After successful dissociation, we checked whether the individual VP1 pentamers were able to form any multimeric structures in the presence of the assembly buffer components (50 mM MOPS, 150 mM NaCl, and 2 mM $CaCl_2$). Up to 19 h after exchanging the VP1 pentamers into the assembly buffer, we only observed free single VP1 pentamers. This indicates that under these conditions, an additional trigger is necessary to initiate assembly.

Empty versus DNA-induced assembly

To obtain empty VLPs, we dialyzed our VP1 pentamers against a high-ionic-strength buffer that has been shown to stimulate the assembly VLPs, 2 M $(NH_4)_2SO_4$ (27). During dialysis, only VP1 pentamers are present, with no other proteins or nucleic acid. Assembly of these VP1 pentamers results in the formation of so-called "empty" VLPs. At different time points, we examined aliquots of the assembly reaction for AFM imaging. After 4.5 h, we observed some ~45 nm VLPs similar to the wild-type SV40 capsid, together with several smaller ~30 nm VLPs and many smaller incomplete structures (Fig. 2 *c*). A similar distribution of VLPs was observed up to 11 h, but after >15 h, these VLPs started aggregating into bigger structures (Fig. 2, *a* and *d*). Thus, the high-ionic-strength buffer, which forces the VP1 pentamers to interact with each other, results in the formation of a heterogeneous population of VLPs.

When assembly is initiated by an "oversized" dsDNA molecule, such as the 48 kbp (kilobase pair) λ or 8.3 kbp pKYB1 DNA—both of which are larger than the wild-type genome—we observe mostly ~45 nm VLPs (Fig. 2, *b* and *e*). Interestingly, up to 8 h of incubation, we observe more individual VLPs, whereas after >15 h, we started observing clusters of multiple VLPs. These clusters consist of multiple individual VLPs arranged in a beads-on-a-string-like fashion with large void areas in between these structures, suggesting the assembly of multiple VLPs on a single DNA molecule (Fig. 2 *f*). However, after >15 h, we also started observing smaller ~30 nm VLPs and larger (>60 nm) structures (Fig. 2 *a*). A possible explanation for the smaller structures could be that later in the reaction, there is not enough DNA available anymore to support the assembly of ~45 nm VLPs; thus, smaller ~30 nm VLPs will be formed. The larger structures could be due to a combination of two or more partial VLPs fused together during assembly. Overall, dsDNA induces a more controlled assembly pathway, leading to a more homogeneous population of ~45 nm VLPs.

We also imaged assembly structures with dsDNA molecules that were shorter than the SV40 wild-type genome: the ~4 kbp pBr322 plasmid and the ~3 kbp pGEM vector. Triggering assembly with these shorter DNA constructs resulted in a bimodal distribution of both ~33 and ~45 nm VLPs after 2–2.5 h of incubation (Fig. S1). The smaller ~33 nm VLPs are in agreement with the smaller ~30 nm VLPs formed after >15 h incubation with either 48 kbp λ or 8.3 kbp pKYB1 DNA, suggesting that in both cases, not enough dsDNA was available to form a VLP of ~45 nm. Interestingly, after 24 h incubation with 3–4 kbp DNA, only ~45 nm VLPs were observed, suggesting that the ~33 nm VLPs had reorganized themselves and incorporated more VP1 pentamers to form a ~45 nm VLP. This suggests that the smaller ~33 nm VLPs are an assembly intermediate state on its way to complete 45 nm VLPs, comparable to the wild-type SV40 capsid. Alternatively, they could be a local energy minimum that slowly matures by dissociation and reassociation. Thus, in the presence of dsDNA, the VP1 pentamers are flexibly bound and can reorganize themselves, resulting over time in the assembly of ~45 nm VLPs, which appear to be the most stable structures.

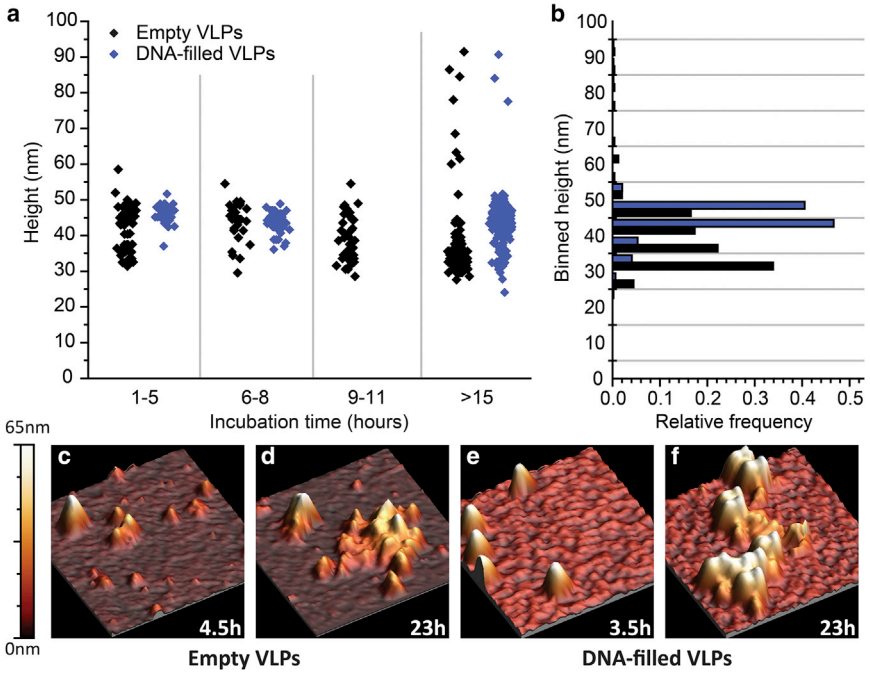

FIGURE 2 In vitro assembly of empty and DNA-filled VLPs. (*a*) A scatter plot representing the height of empty (*black*) and DNA-filled (*blue*) VLPs at several time intervals is shown. Assembly of empty VLPs was induced by dialyzing VP1 pentamers against a high-ionic-strength buffer (2 M $(NH_4)_2SO_4$), and for DNA-filled VLPs, pKYB1 (8.3 kbp) and λ DNA (48 kbp) were used to initiate assembly. All VLPs with a minimal diameter of 15 nm were included from a series of 1 μm^2 images: 230 empty VLPs in 63 images and 490 DNA-filled VLPs in 86 images. (*b*) A histogram of the height of all VLPs from (*a*) is given, showing a more homogeneous population of ~45 nm for DNA-filled VLPs and a more heterogeneous population ranging from 30 to 50 nm for empty VLPs. (*c–f*) Topographical three-dimensional images of assembled VLPs show structures with different heights after 4.5 h (*c*), which become larger, unorganized aggregates after 23 h (*d*). In the case of the DNA-filled VLPs, we observe several ~45 nm VLPs after 3.5 h (*e*) and many ~45 nm VLPs in a beads-on-a-string-like fashion after 23 h (*f*). To see this figure in color, go online.

Mechanical properties of SV40 VP1 VLPs

By performing AFM nanoindentations, we determined the mechanical properties of the in-vitro-assembled empty VLPs, which had a height of ~45 nm, and the in-vitro-assembled DNA-filled VLPs, for which pKYB1 and λ DNA was used. Moreover, the addition of either DTT or EDTA to the cell-derived SV40 VP1 VLPs allowed us to explore the effect of the two major interpentamer interactions (i.e., calcium bridges and disulfide bonds) on the mechanical strength of the cell-derived SV40 VP1 VLPs. From the linear first part of the force-indentation curve, we obtain the spring constant (stiffness) of the VLPs. We observed a bimodal distribution in the stiffness measurements representing a "soft" population of 0.034 ± 0.004 (SD) N/m and a "stiff" population of 0.10 ± 0.01 (SD) N/m (Fig. 3 *a*). In-vitro-assembled empty, in-vitro-assembled DNA-filled, and cell-derived SV40 VLPs, in absence or in presence of DTT or EDTA, display this bimodal distribution. Thus, the two populations are not caused by the absence or presence of DNA nor by the major interpentamer interactions; instead, it could indicate a mixture of intact VLPs and particles with imperfections due to an incomplete assembly process, stress during storage, or stress during immobilization.

To understand this effect, for each particle, we recorded an image before nanoindentation to determine the height, shape, and exact location of the VLP, measured ten consecutive nanoindentation curves, and then obtained another image after nanoindentation to determine the shape and size of the remaining structure (Fig. 4). From these images, we determine the level of damage caused by the nanoindentations. The damage level is represented by the decrease in volume and maximal height of the remaining structure in terms of percentage (Fig. 3 *b*; Table 1). The in-vitro-assembled DNA-filled VLPs showed the least amount of damage, whereas the cell-derived SV40 VLPs in the presence of DTT showed the most visible damage. This highlights a role for the DNA in keeping the VP1 pentamers together in case the interpentamer interactions are disrupted. Imaging of the in-vitro-assembled empty VLPs in the presence of DTT caused these particles to immediately start rupturing; there is clear visible damage before or due to the imaging forces. The level of volume decrease and decrease in maximal height as a result of addition of DTT while imaging was 34 ± 9 and 29 ± 3%, respectively, for in-vitro-assembled empty VLPs, which is similar to cell-derived SV40 VLPs with DTT after nanoindentation, 31 ± 5 and 34 ± 8%, respectively. This shows that the presence of DTT makes the VLPs more prone to damage. A comparison is made between a cell-derived SV40 VLP in absence and presence of DTT in Fig. 4. Both VLPs are round shaped and ~45 nm before nanoindentation. In the absence of DTT, there is a gradual deformation with relative small ruptures seen in the series of nanoindentation curves. In the presence of DTT, there seem to be more drastic rupture events in the first nanoindentation curve. A substantial difference in spring constant is also apparent. Although in the absence of DTT, the second indentation shows a similar slope as the first, in the presence of DTT, the slope of the second indentation is much lower. These effects are consistent with the images obtained after nanoindentation showing a slightly less round ~40 nm VLP in the absence of DTT and a severely damaged structure in case of presence of DTT. Based on the observed damage in the presence of DTT and the less clearly visible damage after

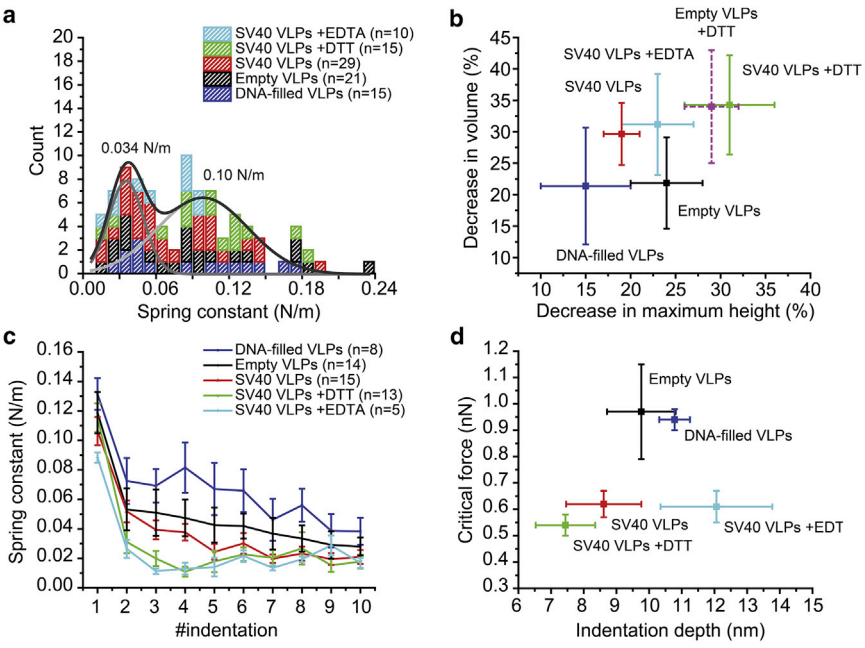

FIGURE 3 Results of AFM nanoindentation experiments on in-vitro-assembled DNA-filled VLPs (*blue*), in-vitro-assembled empty VLPs (*black*), and cell-derived SV40 VLPs in absence (*red*) or presence of 5 mM EDTA (*cyan*) or 2 mM DTT (*green*). (*a*) A histogram of all obtained spring constants shows a softer population of 0.034 ± 0.004 N/m and a stiffer population of 0.10 ± 0.01 N/m (Gaussian fit). (*b*) A scatterplot of the decrease in maximal height versus the decrease in volume in terms of percentage as a result of nanoindentation for all VLPs is shown. See Table 1 for exact numbers. The purple dotted lines represent the amount of damage inflicted by only imaging the empty VLPs in the presence of DTT (volume decrease of 34 ± 9% and decrease in maximal height of 29 ± 3%). (*c*) The trend in the spring constant of the 10 consecutive nanoindentation curves is shown for all intact VLPs. (*d*) A scatterplot of the indentation depth and the force at the critical point for all intact VLPs is shown. See Table 1 for exact numbers. All error bars represent standard error of the mean. To see this figure in color, go online.

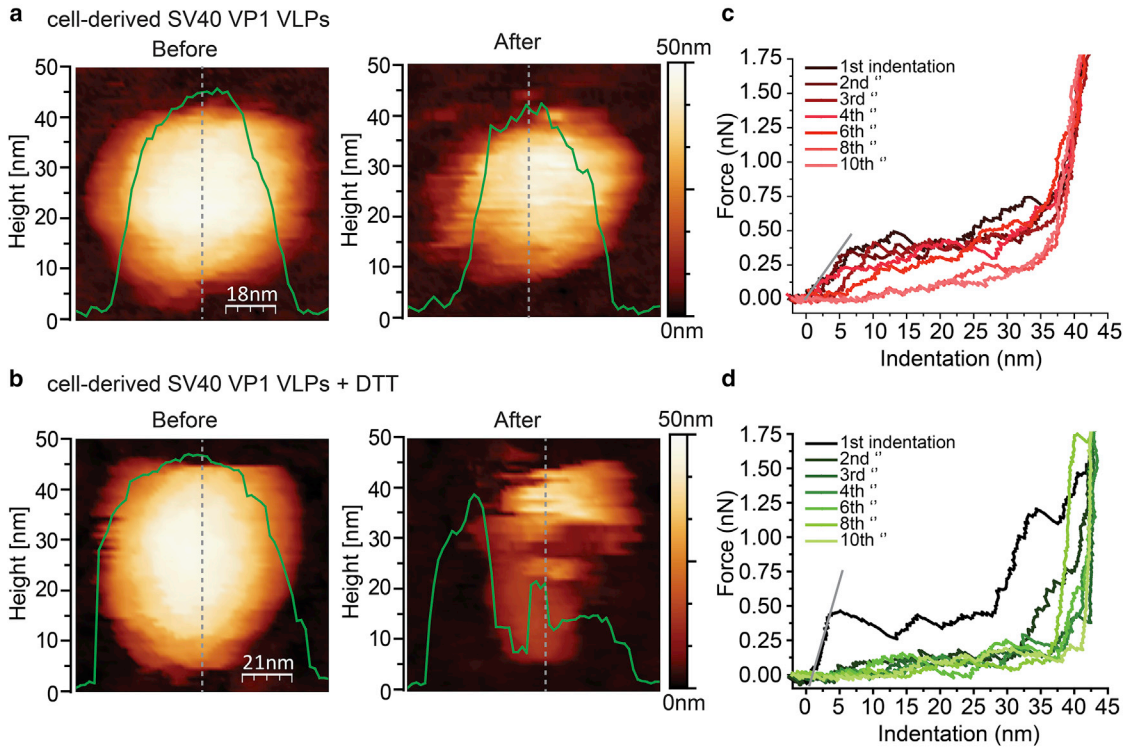

FIGURE 4 Two representative examples of cell-derived SV40 VLPs before and after 10 rounds of nanoindentation in the absence (*a*) and presence (*b*) of 2 mM DTT. The corresponding height profiles (*green line*) along the dotted gray line before and after nanoindentation are overlaid on the images. (*c* and *d*) Seven exemplary indentation curves on the center of a single SV40 VLP are shown. The spring constant is determined from the first linear part of the indentation curves, from the contact point up to the first rupture event with a maximum of the thickness of the shell (~6 nm). These linear regions in the first curves in (*c*) and (*d*) are identified with the gray line. In the absence of DTT (*c*), the VLP gradually deforms upon indentation, with many small recurring rupture events. Recovery occurs during retraction of the tip, resulting in a similar but slightly smoother subsequent indentation curve. The last curve shows the least resistance, indicating a very flexible remaining structure. In the presence of DTT (*d*), several rupture events are observed in the first indentation curve, whereas the consecutive indentation curves are much shallower. Recovery is minimal. The vertical part of the slope at the end of indentation represents cantilever deformation on the solid substrate. To see this figure in color, go online.

nanoindentation in the absence of DTT, we propose an explanation for the bimodal distribution in spring constant: the soft elastic population is correlated with slightly damaged particles, whereas the stiff population corresponds to intact VLPs. This can be confirmed when plotting the spring constant obtained from all second nanoindentation curves showing a single population of ~0.02 N/m (Fig. S2), almost identical to the value of the softer population of ~0.03 N/m obtained from the first nanoindentation curves (Fig. 3 *a*). The VLPs undergo a force-induced structural change in which we believe some interpentamer interactions, possibly hydrophobic interactions, are disrupted, whereas the major interpentamer interactions formed by the more flexible carboxy-terminal arms (21) remain intact, creating a more elastic but morphologically identical VLP.

Next, we plotted the spring constant obtained from each of the ten consecutive nanoindentation curves of the stiffer (initially intact) population of VLPs (Fig. 3 *c*). All VLPs showed a significant drop in spring constant from the first to the second nanoindentation, possibly reflecting the

TABLE 1 Overview of the Measured Properties with AFM Imaging and Nanoindentation

	Decrease in Maximal Height (%)	Decrease in Volume (%)	Spring Constant from First Indentation (N/m)	Critical Force (nN)	Indentation Depth (nm)
DNA-filled VLPs	15 ± 5	21 ± 9	0.13 ± 0.01	1.0 ± 0.2	10 ± 1
Empty VLPs	22 ± 7	24 ± 4	0.12 ± 0.01	0.94 ± 0.04	11 ± 1
SV40 VLPs	19 ± 2	30 ± 5	0.11 ± 0.01	0.62 ± 0.05	9 ± 1
SV40 VLPs + DTT	31 ± 5	34 ± 8	0.12 ± 0.01	0.54 ± 0.05	7 ± 1
SV40 VLPs + EDTA	22 ± 4	31 ± 8	0.088 ± 0.003	0.61 ± 0.06	12 ± 2

For imaging, the total number of used images are 10, 15, 29, 21, and 15 for DNA-filled, empty, SV40, SV40 + DTT, and SV40 + EDTA, respectively. For nanoindentation, a total of 8, 14, 15, 13, and 5 nanoindentation curves were used, respectively, for DNA-filled, empty, SV40, SV40 + DTT, and SV40 + EDTA. Reported values are mean ± standard error of the mean.

abovementioned structural transition. VLPs in the absence of EDTA and DTT showed a gradual decrease in stiffness from the second to 10th nanoindentation. The presence of DTT and EDTA resulted in a steep drop in stiffness up to the third nanoindentation. Overall, both DTT and EDTA seem to destabilize the VLPs, whereas the presence or absence of a genome does not affect the stiffness of the VLPs. We also obtained the indentation depth and critical force, the point at which irreversible deformation occurs (Fig. 3 *d*; Table 1). The highest critical forces were measured on the in-vitro-assembled empty and DNA-filled VLPs. The cell-derived SV40 VLPs, on the other hand, break at a significantly lower force. A major difference between these VLPs is the long-term storage at −20°C of the cell-derived SV40 VLPs, which we thawed on the day of the nanoindentation experiments, whereas for the in-vitro-assembled VLPs, we incubated VP1 pentamers under the appropriate assembly conditions and performed nanoindentations within 30 h after initiation of assembly. Thus, it appears that the cell-derived SV40 VLPs are somewhat damaged/less stable, resulting in a lower critical force, because of the long-term storage. Although the presence of DTT does not significantly change the critical force for the VLPs, the presence of EDTA increases the indentation depth, as expected when the critical force is comparable but the spring constant is lower.

DISCUSSION

In this study, we explored the assembly pathway as well as the mechanical strength of SV40 VLPs. We assembled in vitro both empty VLPs by using a high-ionic-strength buffer and DNA-filled VLPs by using different dsDNA sizes. When we used 3–4 kbp dsDNA to initiate assembly, we observed smaller intermediate ∼33 nm and complete ∼45 nm VLPs after 2–2.5 h, but only ∼45 nm VLPs after 24 h (Fig. S1). The 45 nm particles correspond to the size of the native SV40 capsid. Possibly the DNA used to initiate assembly was too short; when the complete DNA is covered with VP1 pentamers, this might only be enough to form a ∼33 nm VLP. Interestingly, these smaller intermediate VLPs are apparently in a local free-energy minimum, as over time they are able to incorporate additional VP1 pentamers to proceed to the global free-energy minimum for SV40, the complete ∼45 nm VLP. In this scenario, VP1 pentamers in solution can bind the remaining free arms of the already-bound VP1 pentamers independent of DNA binding. We also observed these smaller intermediate structures with "oversized" DNA after 24 h. This would be in agreement with the hypothesis that when multiple VLPs are formed on the same DNA molecule, limited DNA remains available, resulting in smaller intermediate VLPs. We expect these structures to also be able to incorporate more VP1 pentamers over time, resulting in a ∼45 nm VLP. Thus, when 3–4 kbp DNA is used to initiate assembly, smaller ∼33 nm VLPs are formed; however, over time, rearrangement of the already-bound VP1 pentamers is possible to finally reach the more favorable ∼45 nm VLP. Alternatively, the 33 nm diameter is also consistent with a spherical particle arranged with a 42-pentamer $T = 4$ lattice that has been observed with papillomaviruses, which share a pentamer-based architecture (49).

Using a high-ionic-strength buffer to initiate assembly of empty VLPs in vitro resulted in a heterogeneous population of VLPs ranging from ∼30 to ∼50 nm. Interestingly, these ∼30 nm structures were not able to rearrange themselves into 45 nm VLPs but started to aggregate after >15 h. Kanesashi et al. (27) extensively explored the empty assembled structures induced by high salt concentrations, reporting several structures including capsid-like structures similar to the wild-type SV40 capsid (∼40 nm), intermediate particles of 25–35 nm, tiny particles of 20 nm ($T = 1$, consisting of 12 pentamers), and tubular structures. They hypothesized that in empty structures, the carboxy-terminal arms can be fixed into a particular conformation leading to the accumulation of specific kinds of assembly structures, which could explain why we do not observe reorganization of any of the already-formed assembled structures.

When we used "oversized" 48 kbp λ or 8.3 kbp pKYB1 DNA, we observed a homogeneous population of ∼45 nm VLPs. For up to 8 h, these are mostly single VLPs assembled on a DNA molecule. However, pKYB1 and λ DNA are too large to fit inside a single 45 nm VLP, so only part of the DNA is packaged inside the VLP and part of the DNA remains outside. Interestingly, after >15 h, multiple VLPs are assembled in clusters on DNA molecules. This time-dependent behavior indicates that nucleation might be the rate-limiting step. The exact structure of these VLPs with partly packaged DNA remains unresolved. However, their mechanical properties are comparable to the ∼45 nm empty VLPs, which suggests they are complete VLPs consisting of 72 VP1 pentamers. The structure of a SV40 capsid was determined at 3.1 Å resolution (20,21). In the $T = 7$ icosahedral capsid (∼45 nm), VP1 pentamers fill the 12 pentavalent and 60 hexavalent sites. This mismatch of VP1 pentamers and six neighbors might, with minimal disturbance to the capsid structure, leave enough space for the DNA to exit the capsid through related defects in the capsid structure. Thus, the VLPs assembled on λ DNA and pKYB1 DNA most likely consist of 72 VP1 pentamers forming VLPs in which the DNA is able to stick out; nevertheless, the VLPs are as stable as the empty VLPs of ∼45 nm.

We determined the mechanical properties of freshly in-vitro-assembled ∼45 nm VLPs and cell-derived SV40 VLPs to elucidate the influence of DNA, disulfide bridges, and calcium chelation. In some viruses, the genome causes the capsid to become stiffer (35,37,39,50–52). In SV40, when comparing in-vitro-assembled DNA-filled VLPs to empty VLPs, we did not observe an effect of the genome

on capsid stiffness (0.13 ± 0.01 N/m compared to 0.12 ± 0.01 N/m, respectively (Fig. 3; Table 1)). When comparing the damage inflicted by the nanoindentations, less damage was visible in case of the DNA-filled VLPs. This suggests that the DNA is involved in keeping the VP1 pentamers together, making the DNA-filled VLPs more stable. This is in agreement with the observation that empty VLPs start disassembling in the presence of DTT during imaging. This means that the critical force for these empty VLPs in presence of DTT was below the imaging force ($F_{imaging}$ = 0.35 ± 0.02 nN), which is lower than the critical force we obtained for DNA-containing VP1 VLPs in presence of DTT ($F_{critical}$ = 0.54 ± 0.05 nN). Thus, the DNA has no effect on the stiffness of the VLPs; however, the DNA seems involved in keeping the VP1 pentamers together, increasing its stability against large deformations.

The absence of such stiffening effect of the DNA indicates that the elastic behavior of this VLP is dominated by the interpentamer interactions. The presence of EDTA made the VLPs significantly more elastic (0.088 ± 0.003 N/m compared to 0.11 ± 0.01 N/m in the absence of EDTA/DTT and 0.12 ± 0.01 N/m in the presence of DTT (Table 1)). The critical force is similar for all three conditions; therefore, the indentation depth will be increased for the VLPs in the presence of EDTA. Thus, the calcium bridges are involved in the elasticity of the capsid as was previously shown by Llauro et al. (53) for tomato bushy stunt virus. Furthermore, when comparing the shift in stiffness as a function of the consecutive indentations, the initial drop in stiffness is more drastic for the VLPs in the presence of either DTT or EDTA. Additionally, the damage inflicted by nanoindentation is increased in the presence of DTT/EDTA. Thus, both the disulfide bonds and the calcium bridges help stabilize the VLP.

Cieplak et al. (54) simulated the nanoindentation behavior of SV40 and many other viral capsids. Using a coarse-grained structure-based model, they predicted a spring constant of 0.127 N/m and a critical force of 1.43 nN. This simulated spring constant is in agreement with our experimentally obtained data, 0.11 ± 0.01 N/m for the cell-derived SV40 VLPs and 0.13 ± 0.01 and 0.12 ± 0.01 N/m for the in-vitro-assembled DNA-filled and empty VLPs, respectively. This fits with capsid stiffness regulated at the submolecular level by flexible local interactions between rigid body subunits because this is the basis of their coarse-grained model. This would also be in agreement with the altered stiffness upon addition of EDTA that affects these interactions. The simulated break force is higher than the experimentally determined critical force: 1.0 ± 0.2 nN in the case of the empty VLPs. From previous studies, it is known that the break force, or critical force of complex supramolecular assemblies, increases with increasing loading rate (55). For SV40, a ∼500 μm/s indentation velocity was used for the simulations compared to ∼53 nm/s in the nanoindentation experiments, providing at least one factor explaining why the simulated break force is higher than the experimentally measured one.

The major advantage of an in vitro self-assembling system like SV40's is the ease of incorporating nonviral materials into the capsid as opposed to inserting material into a preassembled capsid or engineering an in vivo expression system. Different materials have been encapsulated by SV40 VLPs, including foreign DNA of up to 17.7 kbp (7,10,56). For our in vitro SV40 assembly system, we only used the major capsid protein VP1, whereas in literature, VP2 and VP3 are shown to contribute to the infectivity in vivo (29,57–59). This would be in agreement with research conducted on VP1-coated quantum dots that are reported to reside in the cytoplasm after efficiently infecting human cells but are unable to reach the nucleus (8,9,11,15,17). Therefore, the addition of VP2 and VP3 during assembly should be considered when SV40 VLPs are used as a gene delivery system. SV40 VLPs with and without VP2/VP3 have similar morphology to wild-type SV40 by negative stain electron microscopy (23), and many studies are performed with both SV40 VLPs consisting of only VP1 as well as VP1, VP2, and VP3 (12–14,60–65). Altogether, this shows that SV40 VLPs are an interesting candidate for a targeted drug delivery system, which can be useful for numerous (therapeutic) applications. Based on our results, we suggest that a charged DNA (-like) polymer will stimulate self-assembly of homogeneous particles. In addition, without significant improvement to the SV40 system, long term storage of the VLPs should be avoided.

CONCLUSIONS

We used AFM to determine the time course of assembly of SV40 VP1 pentamers and nanoindentation to help us unravel the importance of the interpentamer interactions and the effect of the presence of DNA on the stiffness and stability of the VLPs. These results broaden our knowledge for the design of viral-based drug and gene delivery systems. We suggest that DNA-induced assembly of a homogeneous population of ∼45 nm VLPs is due to the reorganization of DNA-bound VP1 pentamers; in contrast, high ionic strength induced assembly of a heterogeneous population of VLPs. Nanoindentation showed that the presence of a nucleic acid does not contribute to the stiffness of SV40 VLPs but is involved in keeping the VP1 pentamers together, especially with the DTT-induced or EDTA-induced loss of major interpentamer interactions. Both DTT and EDTA destabilize the VLPs, DTT by making the VLPs less resistant to mechanical stress and thus prone to damage and EDTA by inducing a marked softening. Thus, when SV40 VLPs are used as a vessel for drug delivery, DNA incorporation is not required, but the presence of DNA or some other negatively charged polymer can increase the VLPs' stability, especially in the presence of DTT/EDTA.

SUPPORTING MATERIAL

Two figures are available at http://www.biophysj.org/biophysj/supplemental/S0006-3495(18)31029-4.

AUTHOR CONTRIBUTIONS

A.Z., G.J.L.W., and W.H.R. designed the study. M.G.M.v.R. performed the measurements and analyzed the data. C.L. and A.Z. provided the VP1 proteins. G.J.L.W. and W.H.R. supervised the project. M.G.M.v.R., A.Z., G.J.L.W., and W.H.R. wrote the manuscript. All authors discussed the results and contributed to the final manuscript.

ACKNOWLEDGMENTS

We thank K. Young for technical support (Indiana University, Bloomington, Indiana) and D. Vorselen (Stanford University, California) for providing the home-build MATLAB based nanoindentation analyses program.

This work is funded by the Nederlandse organisatie voor Wetenschappelijk Onderzoek (NWO) through NWO Vidi (to W.H.R.) and Vici (to G.J.L.W.) grants and the Stichting voor Fundamenteel Onderzoek der Materie through Projectruimte grants (to G.J.L.W. and W.H.R.).

REFERENCES

1. Arad, U., E. Zeira, …, A. Oppenheim. 2005. Liver-targeted gene therapy by SV40-based vectors using the hydrodynamic injection method. *Hum. Gene Ther.* 16:361–371.
2. Louboutin, J. P., E. Marusich, …, D. S. Strayer. 2011. Gene transfer to the rhesus monkey brain using SV40-derived vectors is durable and safe. *Gene Ther.* 18:682–691.
3. Strayer, D. S. 1999. Gene therapy using SV40-derived vectors: what does the future hold? *J. Cell. Physiol.* 181:375–384.
4. Strayer, D. S., and J. Milano. 1996. SV40 mediates stable gene transfer in vivo. *Gene Ther.* 3:581–587.
5. Kimchi-Sarfaty, C., N. S. Alexander, …, M. M. Gottesman. 2004. Transduction of multiple cell types using improved conditions for gene delivery and expression of SV40 pseudovirions packaged in vitro. *Biotechniques.* 37:270–275.
6. Kimchi-Sarfaty, C., O. Ben-Nun-Shaul, …, M. M. Gottesman. 2002. In vitro-packaged SV40 pseudovirions as highly efficient vectors for gene transfer. *Hum. Gene Ther.* 13:299–310.
7. Kawano, M., K. Doi, …, H. Handa. 2014. SV40 VP1 major capsid protein in its self-assembled form allows VP1 pentamers to coat various types of artificial beads *in vitro* regardless of their sizes and shapes. *Biotechnol. Rep. (Amst.).* 5:105–111.
8. Li, F., K. Li, …, X. E. Zhang. 2010. Viral coat proteins as flexible nanobuilding-blocks for nanoparticle encapsulation. *Small.* 6:2301–2308.
9. Li, F., Z. P. Zhang, …, X. E. Zhang. 2009. Imaging viral behavior in Mammalian cells with self-assembled capsid-quantum-dot hybrid particles. *Small.* 5:718–726.
10. Tsukamoto, H., M. A. Kawano, …, H. Handa. 2007. Evidence that SV40 VP1-DNA interactions contribute to the assembly of 40-nm spherical viral particles. *Genes Cells.* 12:1267–1279.
11. Wang, T., Z. Zhang, …, X. E. Zhang. 2011. Encapsulation of gold nanoparticles by simian virus 40 capsids. *Nanoscale.* 3:4275–4282.
12. Enomoto, T., M. Kawano, …, H. Handa. 2013. Viral protein-coating of magnetic nanoparticles using simian virus 40 VP1. *J. Biotechnol.* 167:8–15.
13. Kimchi-Sarfaty, C., W. D. Vieira, …, M. M. Gottesman. 2006. SV40 Pseudovirion gene delivery of a toxin to treat human adenocarcinomas in mice. *Cancer Gene Ther.* 13:648–657.
14. Sun, X., W. Li, …, Z. Cui. 2016. In vivo targeting and imaging of atherosclerosis using multifunctional virus-like particles of simian virus 40. *Nano Lett.* 16:6164–6171.
15. Gao, D., X. P. Lin, …, Z. Q. Cui. 2016. Intracellular cargo delivery by virus capsid protein-based vehicles: from nano to micro. *Nanomedicine (Lond.).* 12:365–376.
16. Kitai, Y., H. Fukuda, …, H. Handa. 2011. Cell selective targeting of a simian virus 40 virus-like particle conjugated to epidermal growth factor. *J. Biotechnol.* 155:251–256.
17. Li, F., H. Chen, …, Q. Wang. 2012. Three-dimensional gold nanoparticle clusters with tunable cores templated by a viral protein scaffold. *Small.* 8:3832–3838.
18. Takahashi, R. U., S. N. Kanesashi, …, H. Handa. 2008. Presentation of functional foreign peptides on the surface of SV40 virus-like particles. *J. Biotechnol.* 135:385–392.
19. Mukherjee, S., S. Kler, …, A. Zlotnick. 2010. Uncatalyzed assembly of spherical particles from SV40 VP1 pentamers and linear dsDNA incorporates both low and high cooperativity elements. *Virology.* 397:199–204.
20. Liddington, R. C., Y. Yan, …, S. C. Harrison. 1991. Structure of simian virus 40 at 3.8-A resolution. *Nature.* 354:278–284.
21. Stehle, T., S. J. Gamblin, …, S. C. Harrison. 1996. The structure of simian virus 40 refined at 3.1 A resolution. *Structure.* 4:165–182.
22. Ishizu, K. I., H. Watanabe, …, H. Handa. 2001. Roles of disulfide linkage and calcium ion-mediated interactions in assembly and disassembly of virus-like particles composed of simian virus 40 VP1 capsid protein. *J. Virol.* 75:61–72.
23. Kosukegawa, A., F. Arisaka, …, H. Handa. 1996. Purification and characterization of virus-like particles and pentamers produced by the expression of SV40 capsid proteins in insect cells. *Biochim. Biophys. Acta.* 1290:37–45.
24. Leavitt, A. D., T. M. Roberts, and R. L. Garcea. 1985. Polyoma virus major capsid protein, VP1. Purification after high level expression in Escherichia coli. *J. Biol. Chem.* 260:12803–12809.
25. Sandalon, Z., and A. Oppenheim. 1997. Self-assembly and protein-protein interactions between the SV40 capsid proteins produced in insect cells. *Virology.* 237:414–421.
26. Soussi, T. 1986. DNA-binding properties of the major structural protein of simian virus 40. *J. Virol.* 59:740–742.
27. Kanesashi, S. N., K. Ishizu, …, H. Handa. 2003. Simian virus 40 VP1 capsid protein forms polymorphic assemblies in vitro. *J. Gen. Virol.* 84:1899–1905.
28. Kler, S., J. C. Wang, …, A. Zlotnick. 2013. Scaffold properties are a key determinant of the size and shape of self-assembled virus-derived particles. *ACS Chem. Biol.* 8:2753–2761.
29. Chen, X. S., T. Stehle, and S. C. Harrison. 1998. Interaction of polyomavirus internal protein VP2 with the major capsid protein VP1 and implications for participation of VP2 in viral entry. *EMBO J.* 17:3233–3240.
30. Clever, J., D. A. Dean, and H. Kasamatsu. 1993. Identification of a DNA binding domain in simian virus 40 capsid proteins Vp2 and Vp3. *J. Biol. Chem.* 268:20877–20883.
31. Baclayon, M., G. K. Shoemaker, …, W. H. Roos. 2011. Prestress strengthens the shell of Norwalk virus nanoparticles. *Nano Lett.* 11:4865–4869.
32. Ivanovska, I. L., P. J. de Pablo, …, G. J. Wuite. 2004. Bacteriophage capsids: tough nanoshells with complex elastic properties. *Proc. Natl. Acad. Sci. USA.* 101:7600–7605.
33. Marchetti, M., G. Wuite, and W. H. Roos. 2016. Atomic force microscopy observation and characterization of single virions and virus-like particles by nano-indentation. *Curr. Opin. Virol.* 18:82–88.
34. de Pablo, P. J., and M. G. Mateu. 2013. Mechanical properties of viruses. *Subcell. Biochem.* 68:519–551.
35. Carrasco, C., M. Castellanos, …, M. G. Mateu. 2008. Manipulation of the mechanical properties of a virus by protein engineering. *Proc. Natl. Acad. Sci. USA.* 105:4150–4155.

36. Evilevitch, A., W. H. Roos, …, G. J. Wuite. 2011. Effects of salts on internal DNA pressure and mechanical properties of phage capsids. *J. Mol. Biol.* 405:18–23.

37. Hernando-Pérez, M., R. Miranda, …, P. J. de Pablo. 2012. Direct measurement of phage phi29 stiffness provides evidence of internal pressure. *Small.* 8:2366–2370.

38. Roos, W. H., K. Radtke, …, G. J. Wuite. 2009. Scaffold expulsion and genome packaging trigger stabilization of herpes simplex virus capsids. *Proc. Natl. Acad. Sci. USA.* 106:9673–9678.

39. Snijder, J., C. Uetrecht, …, W. H. Roos. 2013. Probing the biophysical interplay between a viral genome and its capsid. *Nat. Chem.* 5:502–509.

40. Mukherjee, S., M. Abd-El-Latif, …, A. Oppenheim. 2007. High cooperativity of the SV40 major capsid protein VP1 in virus assembly. *PLoS One.* 2:e765.

41. Li, C., A. R. Kneller, …, A. Zlotnick. 2017. Single particle observation of SV40 VP1 polyanion-induced assembly shows that substrate size and structure modulate capsid geometry. *ACS Chem. Biol.* 12:1327–1334.

42. Pace, C. N., F. Vajdos, …, T. Gray. 1995. How to measure and predict the molar absorption coefficient of a protein. *Protein Sci.* 4:2411–2423.

43. Porterfield, J. Z., and A. Zlotnick. 2010. A simple and general method for determining the protein and nucleic acid content of viruses by UV absorbance. *Virology.* 407:281–288.

44. Roos, W. H. 2011. How to perform a nanoindentation experiment on a virus. *Methods Mol. Biol.* 783:251–264.

45. Pablo, P. J. d., J. Colchero, …, A. M. Baro. 1998. Jumping mode scanning force microscopy. *Appl. Phys. Lett.* 73:3300–3302.

46. Yang, H. 2011. Change-point localization and wavelet spectral analysis of single-molecule time series. *In* Single-Molecule Biophysics. John Wiley & Sons, Inc., pp. 217–243.

47. Farge, G., M. Mehmedovic, …, M. Falkenberg. 2014. In vitro-reconstituted nucleoids can block mitochondrial DNA replication and transcription. *Cell Rep.* 8:66–74.

48. Moreno-Herrero, F., J. Colchero, and A. M. Baró. 2003. DNA height in scanning force microscopy. *Ultramicroscopy.* 96:167–174.

49. Mukherjee, S., M. V. Thorsteinsson, …, A. Zlotnick. 2008. A quantitative description of in vitro assembly of human papillomavirus 16 virus-like particles. *J. Mol. Biol.* 381:229–237.

50. Carrasco, C., A. Carreira, …, P. J. de Pablo. 2006. DNA-mediated anisotropic mechanical reinforcement of a virus. *Proc. Natl. Acad. Sci. USA.* 103:13706–13711.

51. Ivanovska, I., G. Wuite, …, A. Evilevitch. 2007. Internal DNA pressure modifies stability of WT phage. *Proc. Natl. Acad. Sci. USA.* 104:9603–9608.

52. Michel, J. P., I. L. Ivanovska, …, C. F. Schmidt. 2006. Nanoindentation studies of full and empty viral capsids and the effects of capsid protein mutations on elasticity and strength. *Proc. Natl. Acad. Sci. USA.* 103:6184–6189.

53. Llauró, A., E. Coppari, …, P. J. de Pablo. 2015. Calcium ions modulate the mechanics of tomato bushy stunt virus. *Biophys. J.* 109:390–397.

54. Cieplak, M., and M. O. Robbins. 2013. Nanoindentation of 35 virus capsids in a molecular model: relating mechanical properties to structure. *PLoS One.* 8:e63640.

55. Snijder, J., I. L. Ivanovska, …, G. J. Wuite. 2012. Probing the impact of loading rate on the mechanical properties of viral nanoparticles. *Micron.* 43:1343–1350.

56. Enomoto, T., I. Kukimoto, …, H. Handa. 2011. In vitro reconstitution of SV40 particles that are composed of VP1/2/3 capsid proteins and nucleosomal DNA and direct efficient gene transfer. *Virology.* 420:1–9.

57. Kawano, M. A., T. Inoue, …, H. Handa. 2006. The VP2/VP3 minor capsid protein of simian virus 40 promotes the in vitro assembly of the major capsid protein VP1 into particles. *J. Biol. Chem.* 281:10164–10173.

58. Nakanishi, A., J. Clever, …, H. Kasamatsu. 1996. Association with capsid proteins promotes nuclear targeting of simian virus 40 DNA. *Proc. Natl. Acad. Sci. USA.* 93:96–100.

59. Nakanishi, A., N. Itoh, …, H. Kasamatsu. 2007. Minor capsid proteins of simian virus 40 are dispensable for nucleocapsid assembly and cell entry but are required for nuclear entry of the viral genome. *J. Virol.* 81:3778–3785.

60. Kawano, M., K. Morikawa, …, M. Matsui. 2014. Chimeric SV40 virus-like particles induce specific cytotoxicity and protective immunity against influenza A virus without the need of adjuvants. *Virology.* 448:159–167.

61. Butin-Israeli, V., N. Drayman, and A. Oppenheim. 2010. Simian virus 40 infection triggers a balanced network that includes apoptotic, survival, and stress pathways. *J. Virol.* 84:3431–3442.

62. Butin-Israeli, V., D. Uzi, …, A. Oppenheim. 2008. DNA-free recombinant SV40 capsids protect mice from acute renal failure by inducing stress response, survival pathway and apoptotic arrest. *PLoS One.* 3:e2998.

63. Kimchi-Sarfaty, C., S. Brittain, …, M. M. Gottesman. 2005. Efficient delivery of RNA interference effectors via in vitro-packaged SV40 pseudovirions. *Hum. Gene Ther.* 16:1110–1115.

64. Macadangdang, B., N. Zhang, …, C. Kimchi-Sarfaty. 2011. Inhibition of multidrug resistance by SV40 pseudovirion delivery of an antigene peptide nucleic acid (PNA) in cultured cells. *PLoS One.* 6:e17981.

65. Rund, D., M. Dagan, …, A. Oppenheim. 1998. Efficient transduction of human hematopoietic cells with the human multidrug resistance gene 1 via SV40 pseudovirions. *Hum. Gene Ther.* 9:649–657.